Chapter 5

Influence of Zn doping on microstructure, dielectric and electrical properties in $Bi_{2/3}Cu_3Ti_4O_{12}$ ceramic synthesized by the semi-wet method

5.1. Introduction

It has been discovered that $CaCu_3Ti_4O_{12}$ (CCTO) is characterized by very high permeability, and it has opened up a new field of science of materials. The complex perovskite structure of $CaCu_3Ti_4O_{12}$ is independent of frequency and temperature [1]. CCTO ceramic has a high dielectric constant (ε_r) and good thermal stability over a broad temperature range. CCTO ceramics are electrically heterogeneous and consist of semiconducting grains with insulating grain boundaries, and its giant dielectric phenomenon is attributed to a grain boundary (internal) barrier layer capacitance rather than an intrinsic property associated with the crystal structure [24]. CCTO is a suitable material for use in electronic components, including multi-layer capacitors, varistors, and resonators. In spite of the significant technological advance, the application of CCTO is limited because of high dielectric loss, which is correlated with the extremes of the electrical conductivity of the grains. Several hypotheses have been given to elucidate the causes of the high dielectric constant [2]. Internal Barrier Layer Capacitance (IBLC) arising from grain boundaries was primarily responsible for high ε_r in CCTO ceramics. Recently, a lot of work has been done with the CCTO ceramics based on the partial substitution of Cu or Ti ions aimed at the improvement of the dielectric properties and the understanding of the origin of the highly-insulating materials [3-5]. Due to the change of the mixed-valence structure, the partial isovalent ion substitution of Zn or Mg to the Cu site of $CaCu_3Ti_4O_{12}$ ceramics, the dielectric response enhancement occurs [6,7]. It was found that ε_r of CCTO was increased as a result of the doping of Mg^{2+} and Zn^{2+} ions on Cu^{2+} sites, while the tan δ was reduced [8-11]. The microstructure of $Mg^{2+}$and Zn^{2+} doped CCTO ceramics is likely attributable to the changes

in the internal properties of the grain boundaries [12,13]. CCTO ceramics have shown the best responses when the oxide mixture of this ceramic is heated at high temperatures i.e. annealing at high temperature [14,15]. Physical deposition methods such as RF sputtering, pulsed laser deposition, chemical gas-phase deposition, and sol-gel methods can be used to develop a thin CCTO film at low temperatures [16, 17]. So far, there have been several mechanisms, which have been proposed to describe the source of the high dielectric constant and low dielectric loss (tan δ) [18-23].The isostructural relationship between $Bi_{2/3}Cu_3Ti_4O_{12}$(BCTO) and CCTO has been described in the literature. It has been found that BCTO ceramics show significant similarities in the dielectric, electrical properties, and large dissimilarity in microstructure to CCTO ceramics. Similar to CCTO, it showed dielectric behavior. It has been found that BCTO ceramics prepared via conventional solid-state reaction, show giant-ε_r values larger than 1.5×10^5 in the low frequency range at room temperature [24]. Because of its low cost, the simplicity of the method, and low reaction temperature, The Semi-wet route is one of the best routes in comparison with other methods [25-27].

In this contribution, we used a semi-wet method to synthesize Zn doped BCTO ceramics. The microstructure, dielectric and electrical properties of BCTO and BCZTO ceramics were studied in detail.

5.2. Materials Synthesis and Characterization

$Bi_{2/3}Cu_{3-x}Zn_xTi_4O_{12}$ (x = *0, 0.05, 0.1, 0.2*), designated as BCTO, BCZTO-0.05, BCZTO-0.1 and BCZTO-0.2, were synthesized by a chemical pathway. First, Bismuth nitrate

$Bi(NO_3)_3.5H_2O$ (99% Merck, India), Copper acetate $Cu(CH_3COO)_2.H_2O$ (99% Merck, India), Zinc acetate $Zn(CH_3COO)_2.H_2O$ (98.5% Merck, India) and Titanium oxide TiO_2 (98.5% Merck, India) were taken in a stoichiometric ratio. $Bi(NO_3)_3.5H_2O$, $Cu(CH_3COO)_2.H_2O$, and $Zn(CH_3COO)_2.H_2O$ were dissolved in distilled water. Then, the stoichiometric amount of solid TiO_2 was mixed with this solution. As a chelating agent, the estimated amount of citric acid (99.5%, Merck India) was mixed with the above solution. The resulting solution was heated using a hotplate magnetic stirrer at 343-353 K to vanish water and allowed for self-ignition. The dry powders of BCTO and BCZTO were obtained after the removal of most of the gases. The resulting BCTO and BCZTO powders were pulverized with a pestle and mortar until fine powders were obtained. The Powders were calcined at 1073 K for 8 h. Cylindrical pellets were prepared using a pressure of 5 tons with a hydraulic press for 90 s. PVA was used (as a binder) to prepare Pellets. This binder was heated at 773 K for 3 h. Finally, BCTO and BCZTO pellets were formed and sintered at 1123 K for 8 h.

The phase formations of the ceramics were examined by using an X-ray Diffractometer (Rigakuminiflex 600, Japan). Microstructure and elemental analysis of all samples were determined by scanning electron microscopy (ZEISS model, EVO-18 research, Germany) and energy-dispersive X-ray spectroscopy (Oxford instruments; Great Britain), respectively. Bright Field TEM images were obtained by Transmission Electron Microscopy (TEM, FEI Tecnai-20G). The FTIR spectra of sintered powder was characterized by ATR FTIR (Bruker, ALPHA model) Spectrophotometer using KBr pellets in the frequency range 500–

1500 cm^{-1}. The oxidation state of the elements present in the ceramic was confirmed by XPS (X-ray Photoelectron Spectroscopy). For dielectric and electrical measurements, cylindrical pellet surfaces were coated with silver paste, and dielectric data were recorded with LCR meter (PSM 1735-NumetriQ, Newton 4th Ltd. UK) in the temperature range of 300-500 K and frequency range of 100 Hz -10 MHz. The copper wire was taken as the current collector and a substrate (carbon paper) was attached to the copper wire with the help of conductive silver glue. The backside of the carbon paper and the exposed part of the copper wire was insulated by using gluestick. Then a dispersion was prepared to have 5 mg of prepared material, 2-propanol of 0.2 mL, Nafion of 12 μL, and drop cast on the carbon paper of 1 cm^2 area. The active mass loading was 2 mg/cm^2. Then the prepared electrode was dried for around half an hour in a vacuum oven till the complete disappearance of the used solvents. cyclic voltammetry (CV) in the three electrode systems of all samples was performed by Versastat 3. In a three-electrode system Ag/AgCl, Platinum, and active material were taken as reference electrodes, a counter electrode, and a working electrode, respectively.

5.3. Results and discussion

5.3.1. X-ray Diffraction (XRD) analysis

The single phase formation of BCTO was observed in the X-ray diffraction patterns of $Bi_{2/3}Cu_{3-x}Zn_xTi_4O_{12}$ ceramics (x=0, 0.05, 0.1, and 0.2), as shown in Fig. 5.1 [24]. The diffraction peaks of BCTO ceramic (JCPDS card no. 46-0725) are found to be (2 0 0), (2 1 1), (2 2 0), (3 1 0), (2 2 2), (3 2 1), (4 0 0), (4 2 2), and (4 4 0) planes as same as CCTO (JCPDS card no. 75-2188). Crystallite size (D) of BCTO and BCZTO ceramics was

calculated by applying Debye-Scherrer formula [18] and the average crystallite size of all ceramics is equal to 40.42 nm.

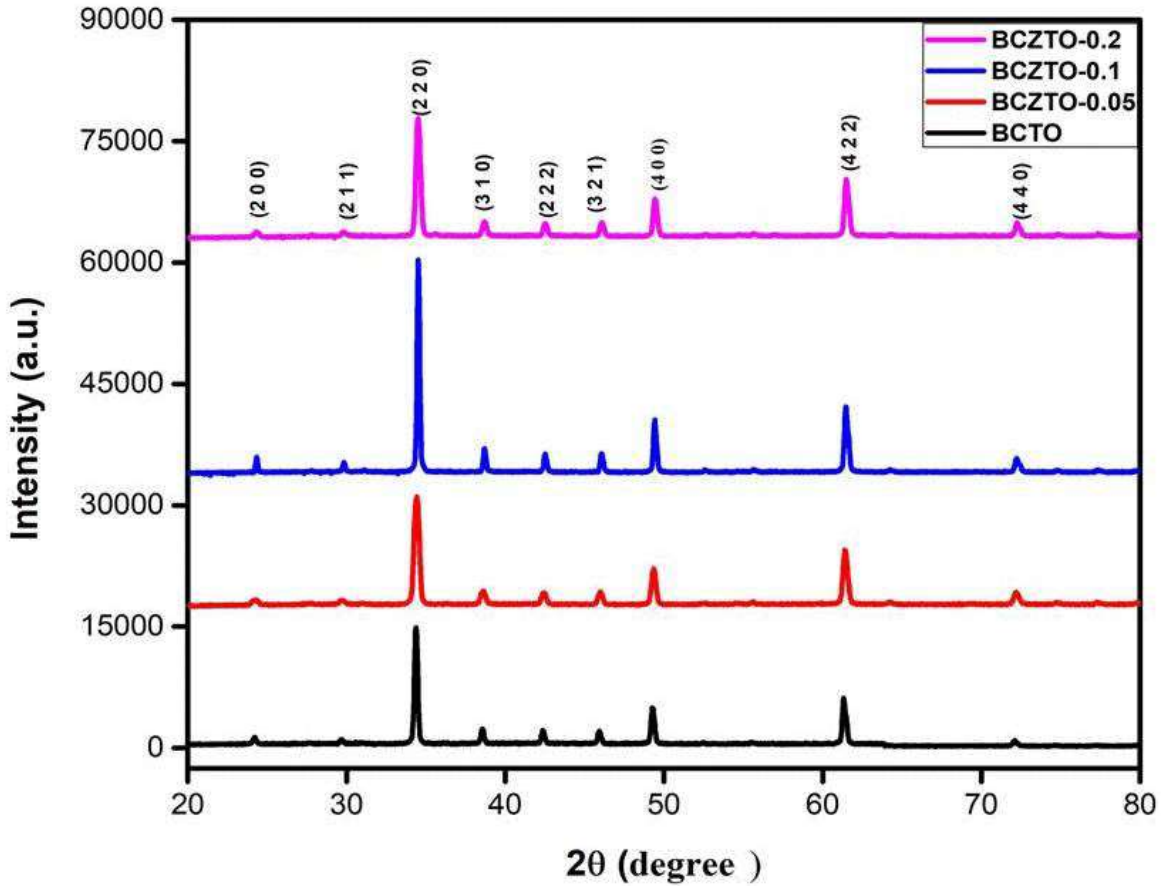

Fig. 5.1. XRD Pattern of BCTO, BCZTO-0.05, BCZTO-0.1 and BCZTO-0.2 ceramics sintered at 1123 K for 8 h.

5.3.2. Microstructural studies

5.3.2.1. Scanning Electron Microscopic (SEM) studies

SEM images of BCTO, BCZTO-0.05, BCZTO-0.1, and BCZTO-0.2 ceramics are shown in Fig. 5.2a-d, respectively. The doping insertion of different concentrations of Zn ions directly interferes with ceramic formation. In the figure of the SEM images, we have seen some

porosity. It also clears from the figures that grains exist in granular form with a polygonal shape which is well parted by grain boundaries. The porosity may be due to gas evolution during the combustion of citrate-nitrate precursor gel. Agglomeration of $Bi_{2/3}Cu_{3-x}Zn_xTi_4O_{12}$ (x= 0, 0.05, 0.1, and 0.2) increased when the concentration of Zn was increased as seen in the figures.

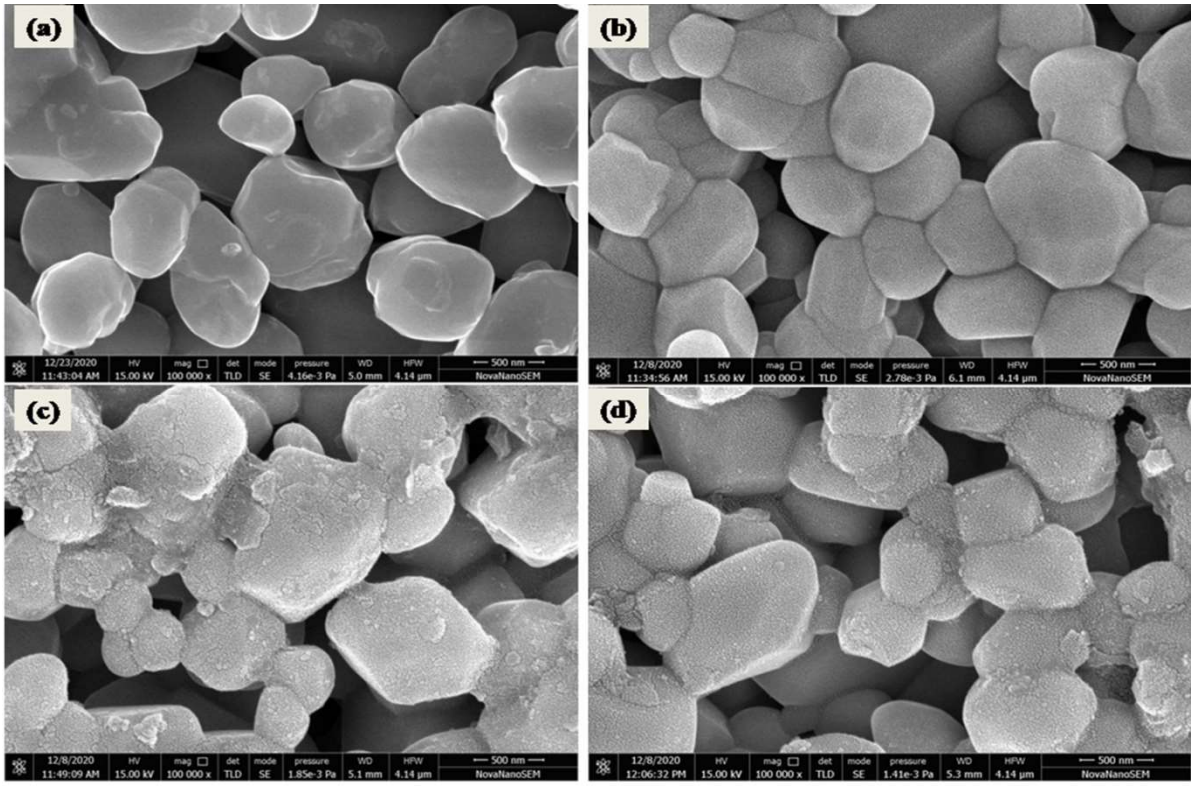

Fig. 5.2 SEM images of **a** BCTO; **b** BCZTO-0.05; **c** BCZTO-0.1;**d** BCZTO-0.2 ceramics.

At the maximum concentration (x = 0.20), as shown in Fig. 5.2d, the highest agglomeration and dense morphology were observed. The average grain sizes of BCTO, BCZTO-0.05, BCZTO-0.1, and BCZTO-0.2 ceramics were found to be 0.70, 0.57, 0.50, and 0.53 μm,

respectively. Fig. 5.3a-d shows EDX spectra of BCTO, BCZTO-0.05, BCZTO-0.1, and BCZTO-0.2 ceramics, respectively. Stoichiometry and purity of above-mentioned samples were examined by EDX data, as given in the tabular form, in Fig. 5.3. From the table given in Fig. 5.3a, the atomic % of Bi, Cu, Ti, and O are 4.22, 18.97, 25.29, and 51.52 respectively, which gives a formula close to $Bi_{2/3}Cu_3Ti_4O_{12}$.

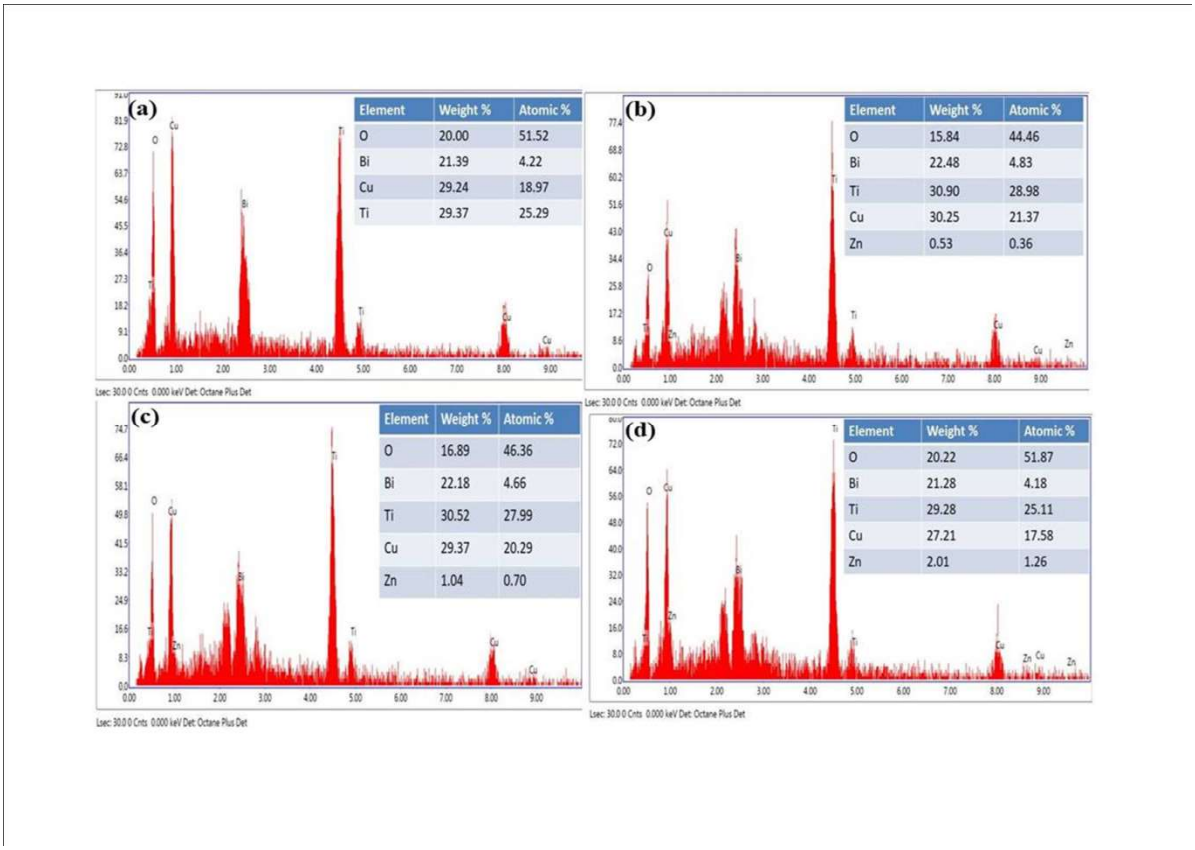

Fig. 5.3 EDX images of **a**BCTO; **b** BCZTO-0.05; **c** BCZTO-0.1; **d** BCZTO-0.2 ceramics.

From the table given in Fig. 5.3b, the atomic % of Bi, Cu, Zn, Ti, and O are 4.83, 21.37, 0.36, 28.98, and 44.46 respectively, which gives a formula close to $Bi_{2/3}Cu_{2.95}Zn_{0.05}Ti_4O_{12}$

(i.e. BCZTO-0.05). From the table given in Fig. 5.3c, the atomic % of Bi, Cu, Zn, Ti, and O are 4.66, 20.29, 27.99, and 46.36 respectively, which gives a formula close to $Bi_{2/3}Cu_{2.9}Zn_{0.1}Ti_4O_{12}$ (i.e. BCZTO-0.1). From the table given in Fig. 5.3d, the atomic % of Bi, Cu, Zn, Ti, and O are 4.18, 17.58, 1.26, 25.11, and 51.87 respectively, which gives a formula close to $Bi_{2/3}Cu_{2.8}Zn_{0.2}Ti_4O_{12}$ (i.e. BCZTO-0.2). Thus, Stoichiometry of all samples was verified by EDX data.

5.3.2.2. Transmission Electron Microscopic (TEM) studies

The bright-field TEM image and SAED patterns of Zn-doped BCTO ceramics are shown in Figs. 5.4 and 5.5. The particle size was calculated from bright-field TEM, shown in Fig. 5.4a, b, and Fig. 5.5a. It was found at 43.19 nm, 54.68 nm and 64.60 nm for BCZTO-0.05, BCZTO-0.1, and BCZTO-0.2 ceramics respectively. It is observed that particle size increases with an increase in Zn concentration due to particle agglomeration [31].

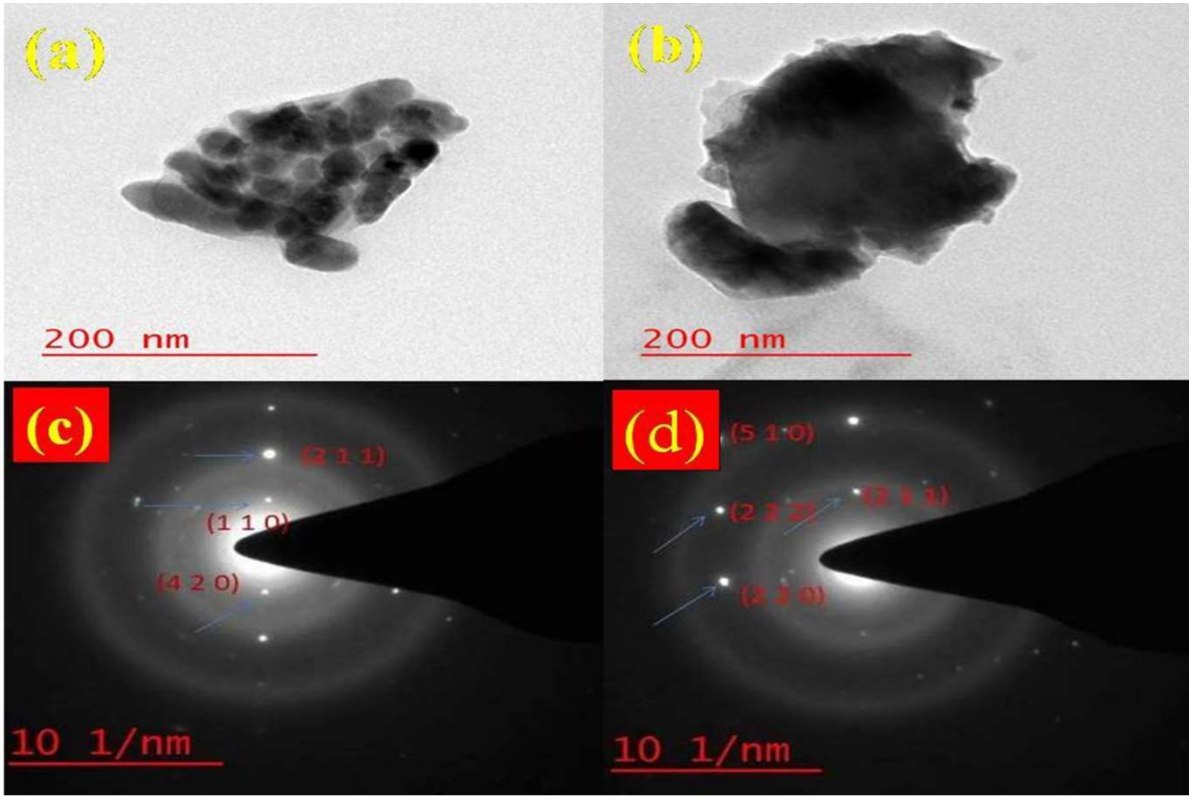

Fig. 5.4 a and b Bright-field TEM images;**c and d** SAED pattern of BCZTO-0.05, BCZTO-0.1ceramics respectively.

The nature of particles was found to be crystalline, which can be seen from Figs. 5.4a, 5.4b, and 5.5a. Figs. 5.4c, 5.4d, and 5.5b display the Selected Area Electron Diffraction (SAED)

patterns of BCZTO-0.05, BCZTO-0.1, and BCZTO-0.2 ceramics respectively.

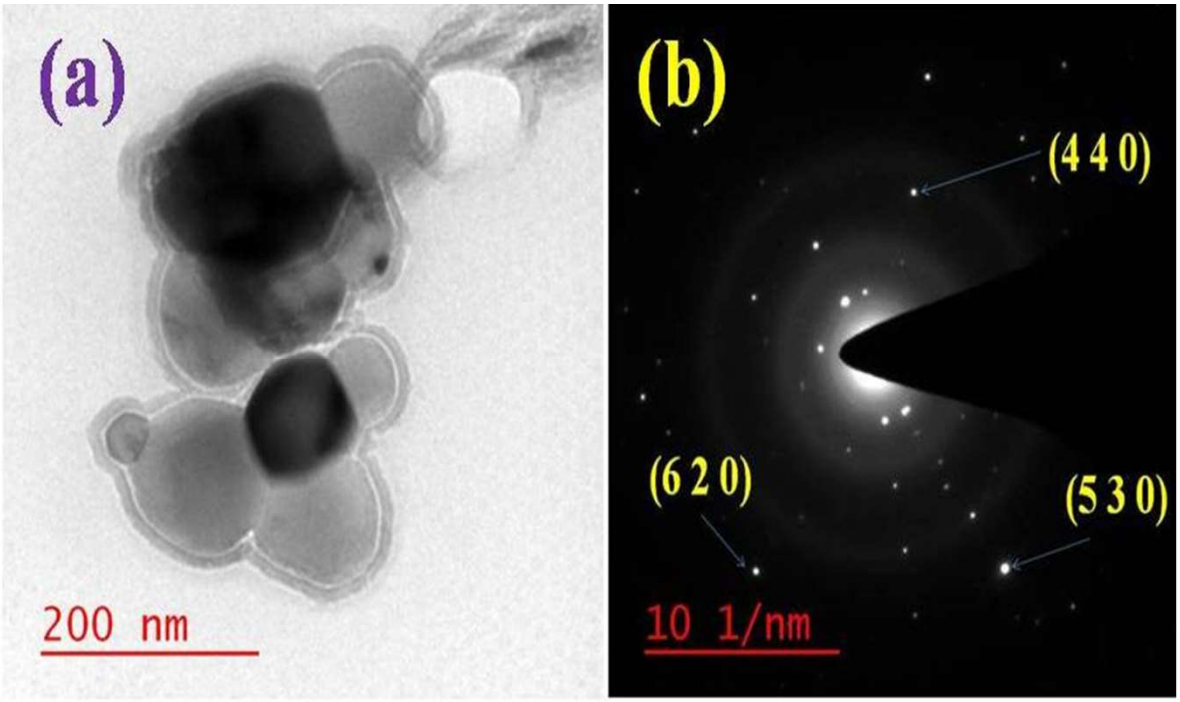

Fig . 5.5a Bright-field TEM image; **b** SAED pattern of BCZTO-0.2 ceramic.

The crystal planes in the SAED pattern of the ceramics are indicated. The incidence of the bright spot pattern in the SAED pattern shows the nano-crystalline nature of the particles.

5.3.3. X-Ray Photoelectron Spectroscopic (XPS) studies

The oxidation states of the elements present in the BCZTO-0.2 ceramic are confirmed by X-Ray Photoelectron Spectroscopy (XPS) Studies. The XPS spectra of BCZTO-0.2 ceramic

are shown in Fig. 5.6.

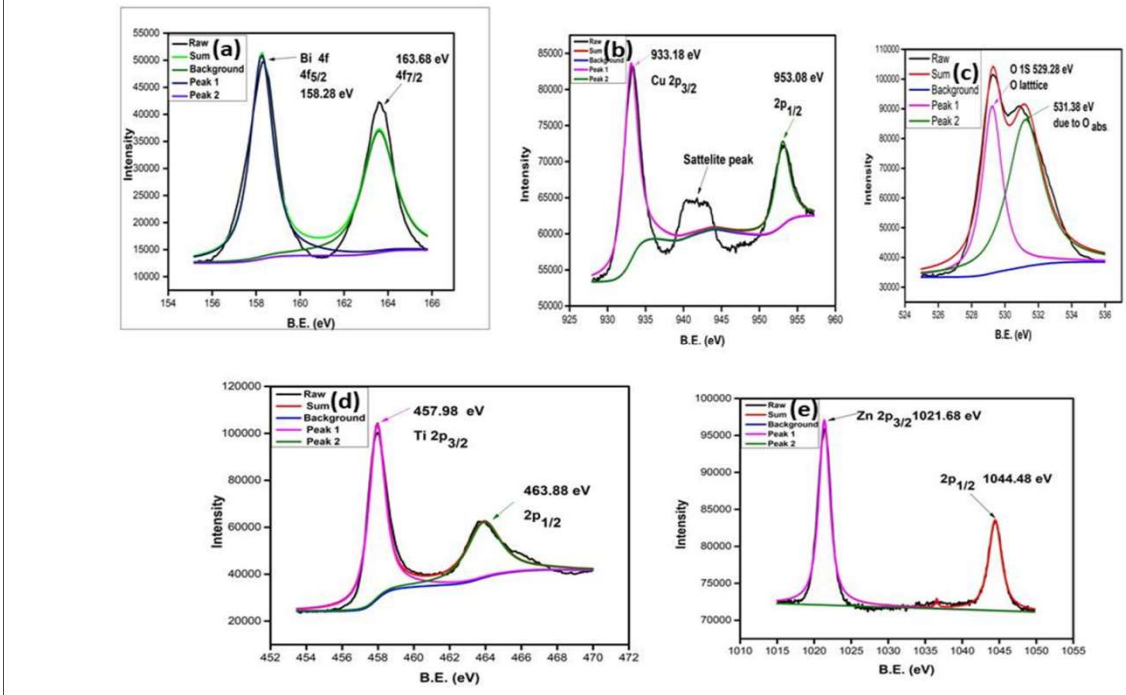

Fig. 5.6 XPS spectra of **a** Bi;**b** Cu; **c** O; **d** Ti; **e** Zn of BCZTO-0.2 ceramic.

In this ceramic, Bi, Cu, O, Ti and Zn elements are present and its XPS spectra are shown in Fig. 5.6a, b, c, d, and e, respectively. In Fig. 5.6a, two peaks at binding energies of 159.1 and 164.5 eV are correlated to Bi $^4f_{5/2}$ and Bi $^4f_{7/2}$, respectively, which confirms the presence of Bi^{3+}. The peak positions of Cu, Ti, O, and Zn observed in Fig. 5.6b, c, d and e confirm the oxidation states of +2, +4, -2, and +2, respectively [20-23].

5.3.4. Dielectric studies

Fig. 5.7a demonstrates the dependence of dielectric permittivity (ε_r) on the frequency at 310 K for the undoped and Zn-doped BCTO ceramics. In the figure, the variation of dielectric permittivity with frequency is almost the same for all the ceramics. It is concluded that the dielectric constant is optimum in the low-frequency region while with increasing frequency, the dielectric constant decreases and remains constant in the higher frequency region [37]. In the low frequency region, space charge polarization occurs. This is due to the rapid periodic reversal of the electric field, which prevents ion diffusions in the direction of the field. The dielectric constant (ε_r) values for BCTO, BCTZTO-0.05, BCZTO-0.1, and BCZTO-0.2 ceramics were measured as 356, 458, 189, and 243, respectively, at 310 K and 100 Hz.

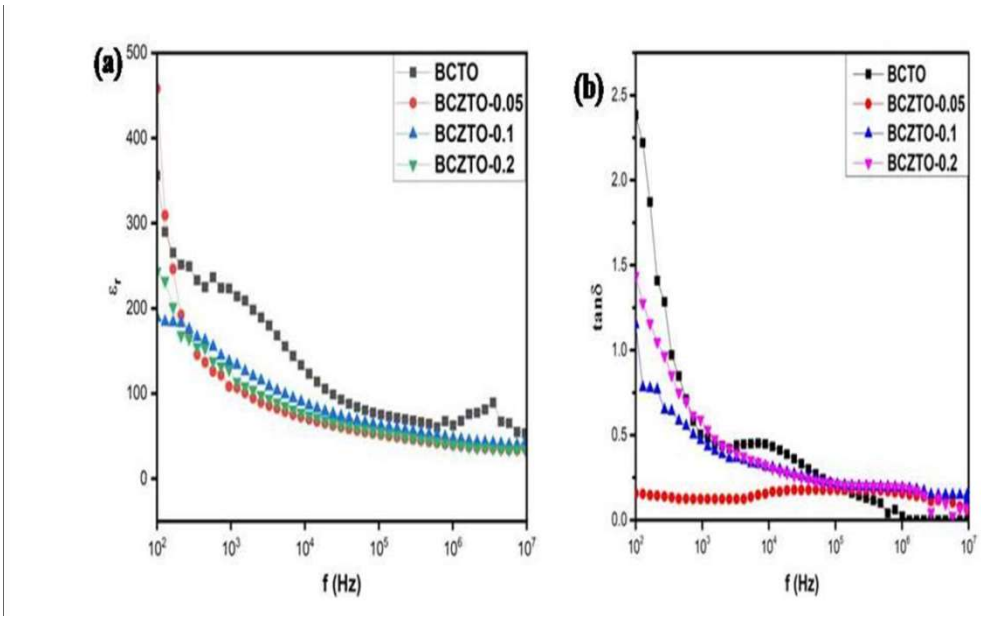

Fig. 5.7 Variation of **a** dielectric constant (ε_r) and **b** tangent loss (tan δ) with frequency at 310 K for BCTO, BCZTO-0.05**,** BCZTO-0.1, and BCZTO-0.2 ceramics.

The highest dielectric constant was found in the BCZTO-0.05 sample. The variation of tangent loss (tan δ) with the frequency of samples BCTO, BCZTO-0.05, BCZTO-0.1, and BCZTO-0.2 at a few selected temperatures is shown in Fig. 5.7b. In BCTO and BCZTO-0.05, the relaxation peaks [32] are observed, while in BCZTO-0.1 and BCZTO-0.2, the relaxation peaks may be observed only below 100 Hz. The dielectric loss is the lowest for the BCZTO-0.05 (0.24), and, also, high dielectric constant is observed for this sample. The tan δ values of BCTO, BCZTO-0.05, BCZTO-0.1, and BCZTO-0.2 ceramics are found to be 0.47, 0.24, 0.37, and 0.53, respectively, at 310 K and 10 kHz. The dielectric constant (ε_r) vs temperature (T) plot at 10 kHz in the undoped and Zn-doped BCTO ceramics is shown in Fig. 5.8a.

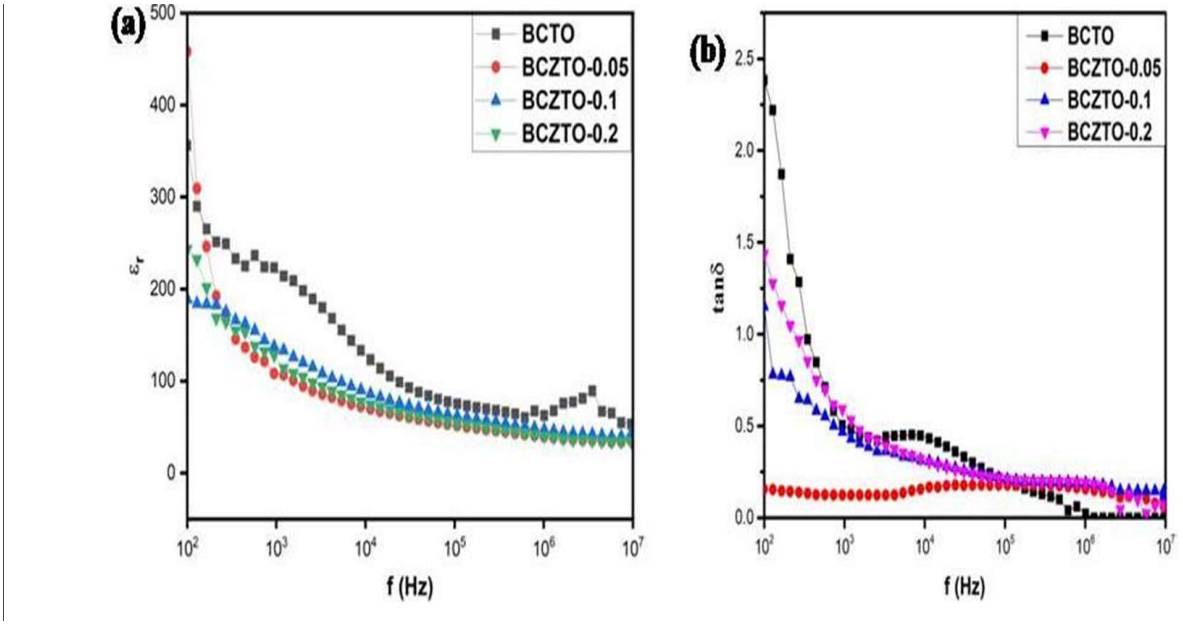

Fig. 5.8 Variation of **a** dielectric constant(ε_r) and **b** tangent loss (tan δ) with temperature at 10 kHz for BCTO, BCZTO-0.05**,** BCZTO-0.1, and BCZTO-0.2 ceramics.

It is observed that the dielectric permittivity is nearly constant up to 500 K at measured frequency [38]. It is concluded that, among the measured samples, the dielectric constant is the highest in BCZTO-0.05. Dielectric loss vs temperature (T) plots for BCTO, BCZTO-0.05, BCZTO-0.1, and BCZTO-0.2 ceramics at fixed frequency are given in Fig. 5.8b.The value of tan$\delta$is nearly independent of temperature up to 500 K. It is seen in Fig. 5.8b that the tangent loss is the lowest in the case of BCZTO-0.05 ceramic among all the measured samples.

5.3.5. Impedance Spectroscopic studies

The complex impedance plot or Nyquist plot (Z″ vs Z′) at 350 K of Zn-doped and un-doped BCTO ceramics is shown in Fig. 5.9a-d.

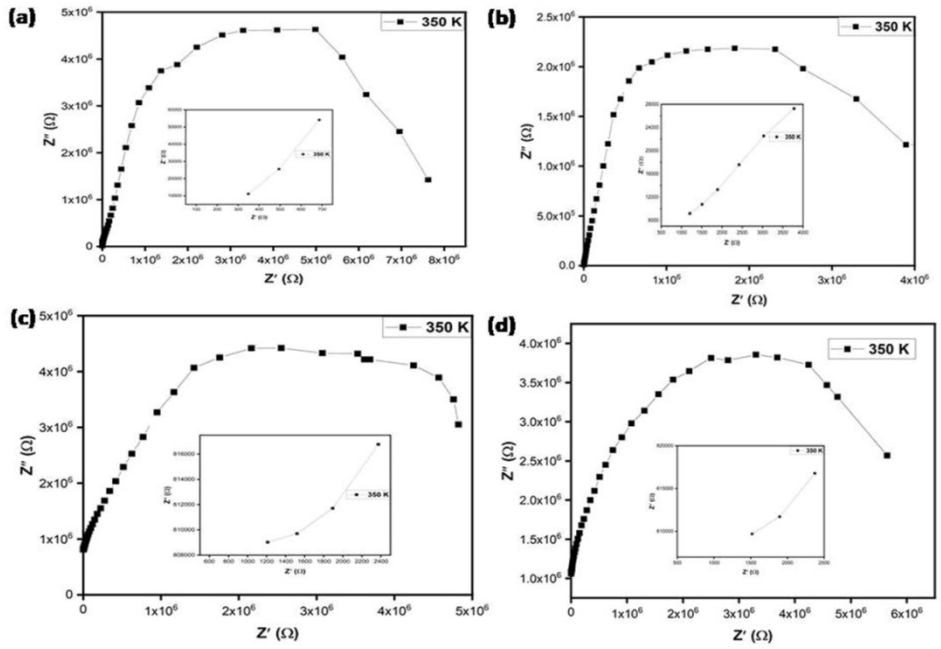

Sample name	**grain Resistance (R_g) (Ω)**	**grain boundary Resistance (R_{gb}) (MΩ)**
BCTO	280	8.8
BCZTO-0.05	800	5.2
BCZTO-0.1	700	5.1

Fig. 5.9 Complex impedance plot or Nyquist plot (Z″ vs Z′) at 350 K for **a** BCTO; **b** BCZTO-0.05; **c** BCZTO-0.1; **d** BCZTO-0.2 ceramics.

Table 5.1 The data of grain and grain boundary resistance for Zn-doped and un-doped BCTO ceramics at 350 K.

The semicircular arc is observed in all the measured samples, which indicates the grain boundary effect. The semicircular arcs for grains at high frequency get reduced due to the high value of grain boundary resistance. The grain resistance is calculated by inset figures, recorded in the high-frequency region. The data of grain and grain boundary resistances at

BCZTO-0.2	900	8.1

It is also observed that the resistance of grain and grain boundaries are semiconducting. The variation of the imaginary part of impedance (Z″) with frequency at selected temperatures is shown in Fig. 5.10a-d for BCTO, BCZTO-0.05, BCZTO-0.1, and BCZTO-0.2, respectively.

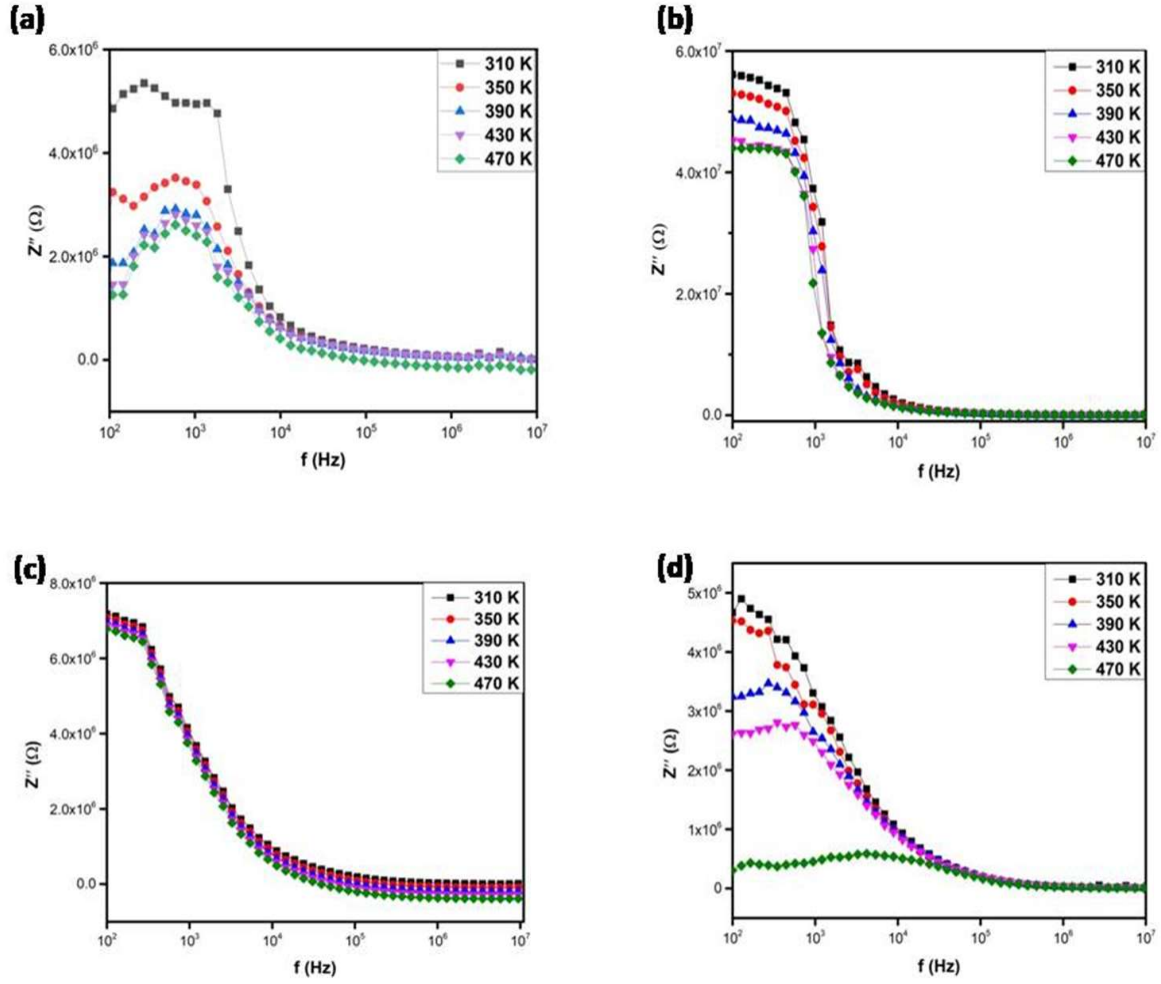

Fig. 5.10 Frequency dependence of imaginary part of impedance (Z″) at selected temperatures for **a**BCTO; **b** BCZTO-0.05;**c** BCZTO-0.1; **d** BCZTO-0.2 ceramics.

The magnitude of Z″ decreases with increasing temperature. It shows the appearance of relaxation peaks. The relaxation peaks were noticed at a lower frequency and peak suppression was reached at higher frequencies. This confirms the existence of the relaxation phenomenon of ceramics [39].

5.3.6. Electrical conductivity

The variation of ln of conductivity (σ) as a function of 1000/T (K^{-1}) at selected frequencies for Zn-doped and undoped BCTO ceramics is shown in Fig. 5.11a-d.

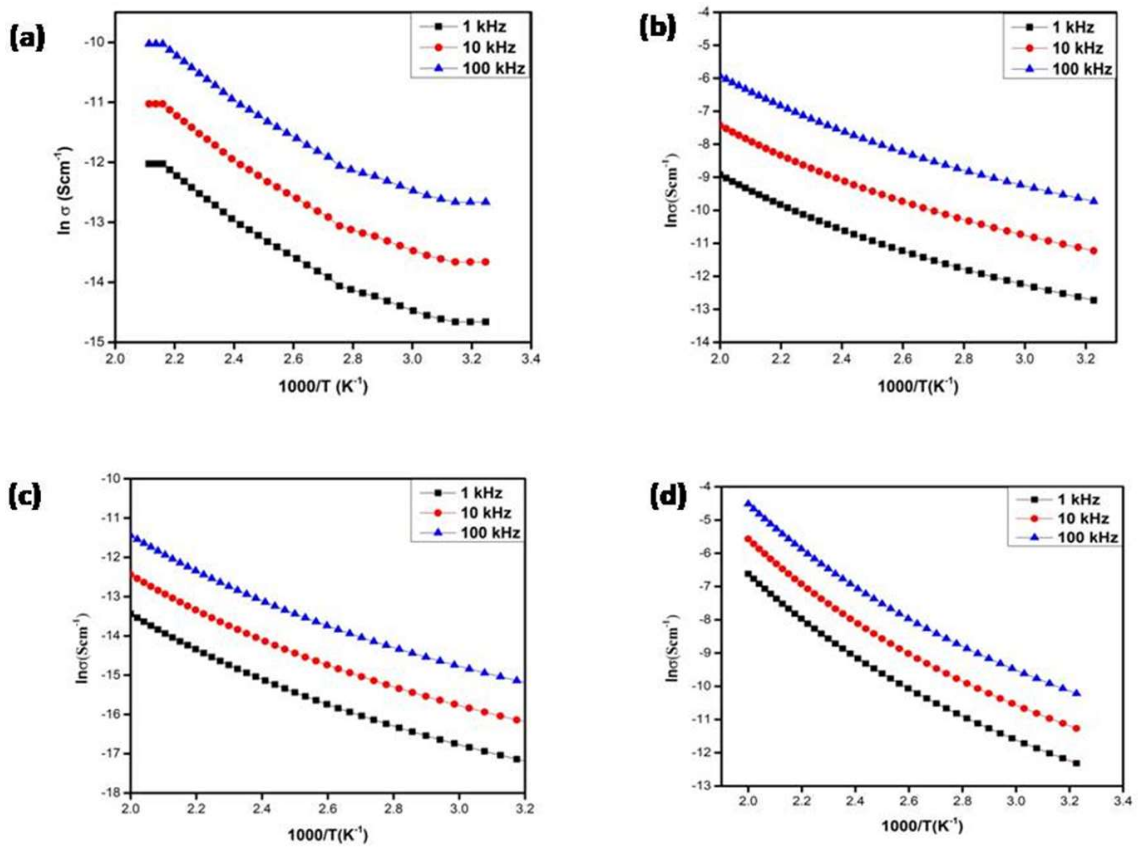

Fig. 5.11 Plots of conductivity (ln σ) with the inverse of temperature at selected frequencies for **a** BCTO;**b** BCZTO-0.05;**c** BCZTO-0.1; **d**BCZTO-0.2 ceramics.

It is observed from the figure that on increasing temperature, the conductivity behavior of the ceramics linearly increases. The temperature dependence of conductivity obeys the Arrhenius law. The activation energy for conduction is measured by the slope of the plot of ln σ vs 1000/Tat 1 kHz. The calculated activation energy for BCTO, BCZTO-0.05, BCZTO-0.1, and BCZTO-0.2 ceramics is found to be 0.25, 0.20, 0.27, and 0.36 eV, respectively.

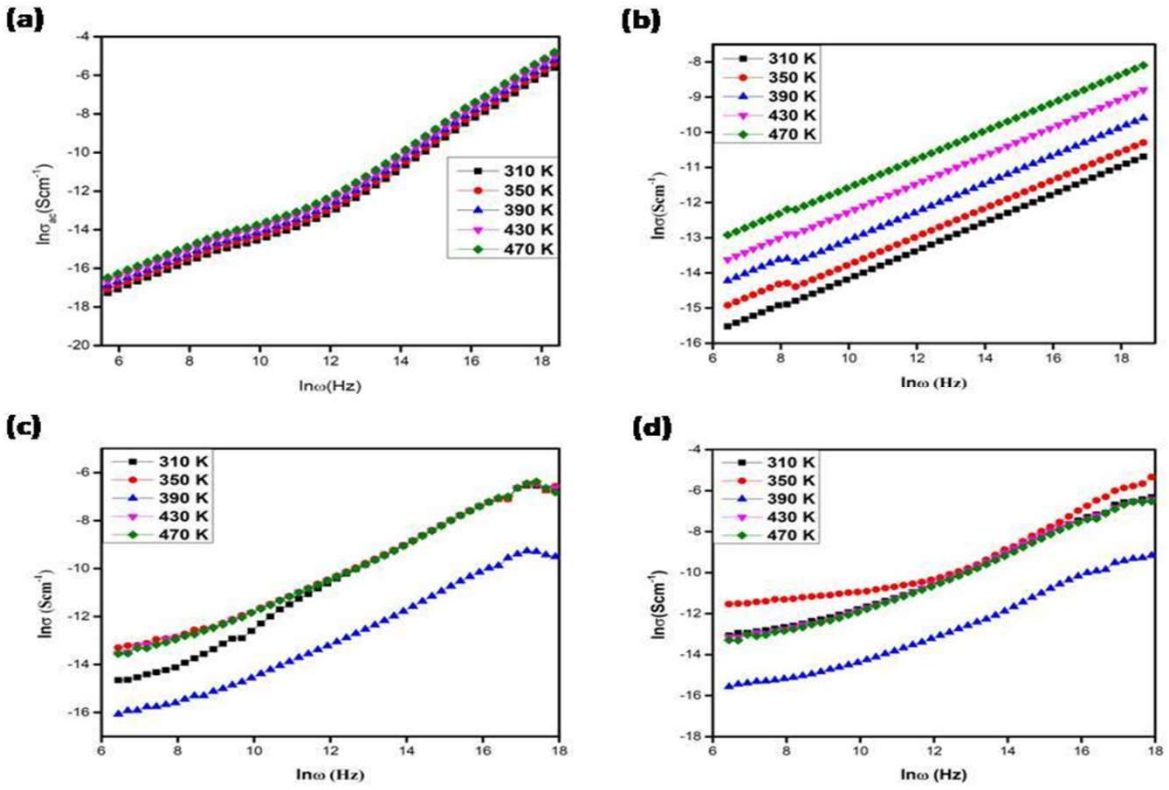

Fig. 5.12 Frequency dependence of AC conductivity (ln σ_{ac}) at selected temperatures for **a** BCTO; **b** BCZTO-0.05; **c** BCZTO-0.1; **d** BCZTO-0.2 ceramics.

The variation of AC conductivity with frequency for BCTO, BCZTO-0.05, BCZTO-0.1, and BCZTO-0.2 ceramics is shown in Fig. 5.12a-d. The frequency-dependent conductivity can be described by the Jonscher power law [40]

$$\sigma(\omega)=\sigma_0+A\omega^s \qquad (5.1)$$

Where A is a constant and s is the power-law exponent.

The AC conductivity [41-44] primarily depends upon frequency. The value of power-law exponent (s) was calculated by the slope of the curve for all measured samples at the temperatures 310 K, 390 K, and 470 K, as shown in Table 5.2. It was observed from table 5.2 that on increasing temperature, s value decreases for all the measured samples.

Table 5.2 The value of power law exponent (s) for BCTO, BCZTO-0.05, BCZTO-0.1, and BCZTO-0.2 ceramics at few selected temperatures.

Ceramic Samples	T= 310 K	T= 390 K	T= 470 K
BCTO	1.18	1.15	1.14
BCZTO-0.05	0.43	0.42	0.41
BCZTO-0.1	0.83	0.82	0.81
BCZTO-0.2	0.73	0.68	0.65

The conductivity mechanism in the ceramics is governed by the thermally activated hopping between two sites separated by an associate energy barrier at the grain boundary. The dielectric conduction process is temperature dependent, related to the hopping of charge carriers [45].

5.3.7. Cyclic Voltammetry

Fig. 5.13 displays the cyclic voltammetry, which was performed in three electrode system [46].These three-electrode systems of Ag/AgCl, platinum and active metal were chosen as the reference electrode, counter electrode and working electrode, respectively. Cyclic Voltammetry of BCTO, BCZTO-0.05, BCZTO-0.1, and BCZTO-0.2 ceramics were performed at a scan rate of 2 mV/s. Two types of mechanisms are observed in the case of supercapacitors, i.e., EDLC (electrical double layer capacitive) and pseudo capacitive. In case of EDLC, the charges are stored in the form of surface adsorption-desorption. Pseudo capacitive materials store charge in form of redox transitions. All the ceramics are pscheudocapative in nature, which can be seen from the CV plot, shown in Fig. 5.13a-d. In But in the figure, it can be seen that the curves are not rectangular which suggest the pseudo capacitive nature of the systems. The maximum currents generated for BCTO, BCZTO-0.05, BCZTO-0.1, and BCZTO-0.2 ceramics are 11.06 mA, 1.37 mA, 1.98 mA, and 67.8 μA, respectively, and the corresponding voltages are 0.996, 0.994, 0.911 and 0.80 V.

In case of ideal capacitors, the CV curves are rectangular in shape.

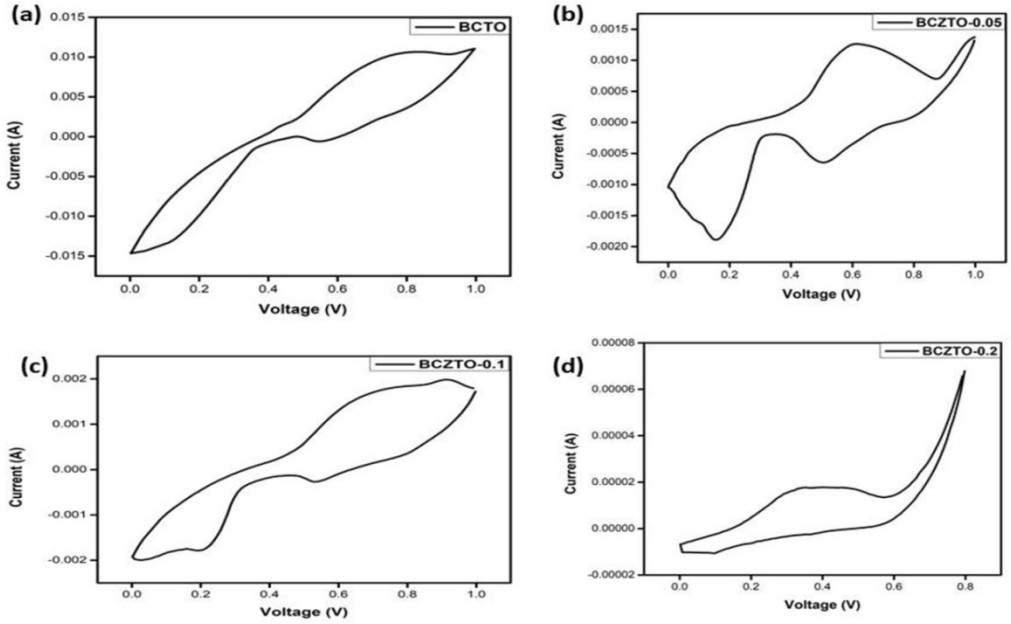

Fig. 5.13 Cyclic Voltammetry plots for **a** BCTO; **b** BCZTO-0.05; **c** BCZTO-0.1; **d** BCZTO-0.2 ceramics.

5.4. Conclusions

The undoped and Zn-doped BCTO ceramics were synthesized by a semi-wet process and sintered at 1123 K for 8 h. The XRD analysis verified the single-phase formation of BCTO and BCZTO ceramics. The crystallite size of $Bi_{2/3}Cu_{3-x}Zn_xTi_4O_{12}$ (x = *0, 0.05, 0.1, 0.2*) ceramics, as observed by XRD is in the range of 45 ± 5 nm. The average particle size of all ceramics was found 60 ± 5 nm by TEM analysis. The oxidation states of the constituent elements in the BCZTO-0.2 ceramic were confirmed by XPS. The dielectric constant of BCTO, BCZTO-0.05, BCZTO-0.1, and BCZTO-0.2 ceramics were found as 356, 489, 189, and 243 at 100 Hz and 470 K. The tangent loss was measured as lowest (0.24) in the case of

BCZTO-0.05 ceramic at 10 kHz and 310 K. The existence of grain and grain boundary effects was confirmed by impedance analysis of BCTO and BCZTO ceramics.The conductivity of BCZTO ceramics increases with an increase in temperature obeying the Arrhenius law. The AC conductivity of BCZTO ceramics increases with increasing frequency, according to the Johncher power law. For Electrochemical characteristics, Cyclic Voltammetry was operated for BCTO, BCZTO-0.05, BCZTO-0.1, and BCZTO-0.2 ceramics and the maximum generated current was found to be 11.06 mA, 1.37 mA, 1.98 mA, and 67.8 µA respectively.

References:

1. Singh, L., Rai, U.S. and Mandal, K.D. (2012). Influence of Zn doping on microstructures and dielectric properties in $CaCu_3Ti_4O_{12}$ ceramic synthesised by semiwet route. *Advances in Applied Ceramics*, 111(7), 374-380.

2. Yadav, B., Kar, K.K., Ghorai, M.K., Kumar, D. and Yadav, D. (2022). Impact of defect migration on electrical and dielectric properties in molten salt synthesized $CaCu_3Ti_4O_{12}$ and customizing the properties by compositional engineering with Mg doping. *Materials Chemistry and Physics*, 281, 125893.

3. Guo, Y., Tan, J. and Zhao, J. (2023). Study on the giant dielectric response of $CaCu_3Ti_{4.2}O_{12-x}NaF$ composite ceramics. *Inorganic Chemistry Communications*, 149, 110358.

4. Singh, P., Laishram, R., Sharma, P. and Kolte, J. (2021). Giant magneto capacitance in magnetoelectric BNT/NFO particulate composites. *Journal of Materials Science: Materials in Electronics*, 32, 21288-21296.

5. Yadav, B., Sinha, P., Kar, K.K., Ghorai, M.K. and Kumar, D. (2022). Exploring the electrical behavior of iodine substituted $CaCu_3Ti_4O_{12-x}I_x$ by impedance and modulus spectroscopy. *Journal of Physics and Chemistry of Solids*, 164,110613.

6. Rai, A.K., Mandal, K.D., Kumar, D. and Parkash, O. (2010). Dielectric properties of $CaCu_3Ti_{4-x}Co_xO_{12}$ (x= 0.10, 0.20, and 0.30) synthesized by semi-wet route. *Materials Chemistry and Physics*, 122(1), 217-223.

7. Espinoza-González, R. and Mosquera, E. (2017). Influence of micro-and nanoparticles of zirconium oxides on the dielectric properties of $CaCu_3Ti_4O_{12}$. *Ceramics International*, 43(17), 14659-14665.

8. Singh, L., Rai, U.S., Rai, A.K. and Mandal, K.D. (2013). Sintering effects on dielectric properties of Zn-doped $CaCu_3Ti_4O_{12}$ ceramic synthesized by modified sol-gel route. *Electronic Materials Letters*, 9, 107-113.

9. Sahoo, S., 2018. Enhanced time response and temperature sensing behavior of thermistor using Zn-doped $CaTiO_3$ nanoparticles. *Journal of Advanced Ceramics*, 7(2), 99-108.

10. Ni, L. and Chen, X.M. (2009). Enhanced giant dielectric response in Mg-substituted $CaCu_3Ti_4O_{12}$ ceramics. *Solid state communications*, 149(9-10), 379-383.

11. Wang, X., Liang, P., Peng, Z., Peng, H., Xiang, Y., Chao, X. and Yang, Z. (2019). Significantly enhanced breakdown electric field in Zn-doped $Y_{2/3}Cu_3Ti_4O_{12}$ ceramics. *Journal of Alloys and Compounds*, 778, 391-397.

12. Ni, L. and Chen, X.M. (2010). Enhancement of giant dielectric response in $CaCu_3Ti_4O_{12}$ ceramics by Zn substitution. *Journal of the American Ceramic Society*, 93(1), 184-189.

13. Wu, Y., Li, J., Huang, H., Bai, H., Hong, Y., Shi, K. and Zhou, Z. (2017). Dual-relaxation-induced tunable colossal dielectric behavior of doped $(Ca_{0.6}Sr_{0.4})_{1.15}Tb_{1.85}Fe_2O_7$ ceramics. *Ceramics International*, 43(15), 13013-13019.

14. Boonlakhorn, J., Kidkhunthod, P., Chanlek, N. and Thongbai, P. (2017). Effects of DC bias on dielectric and electrical responses in (Y+ Zn) co-doped $CaCu_3Ti_4O_{12}$ perovskite oxides. *Journal of Materials Science: Materials in Electronics*, 28, 4695-4701.

15. Mao, P., Wang, J., Xiao, P., Zhang, L., Kang, F. and Gong, H. (2021). Colossal dielectric response and relaxation behavior in novel system of Zr^{4+} and Nb^{5+} co-substituted $CaCu_3Ti_4O_{12}$ ceramics. *Ceramics International*, 47(1), 111-120.

16. Prakash, B.S., Varma, K.B.R., Michau, D. and Maglione, M. (2008). Deposition and dielectric properties of $CaCu_3Ti_4O_{12}$ thin films deposited on Pt/Ti/SiO_2/Si substrates using radio frequency magnetron sputtering. *Thin Solid Films*, 516(10), 2874-2880.

17. Han, C.S., Choi, H.R., Choi, H.J. and Cho, Y.S. (2017). Origin of abnormal dielectric behavior and chemical states in amorphous $CaCu_3Ti_4O_{12}$ thin films on a flexible polymer substrate. *Chemistry of Materials*, 29(14), 5915-5921.

18. Fang, L. and Shen, M. (2008). Effect of laser fluence on the microstructure and dielectric properties of pulsed laser-deposited $CaCu_3Ti_4O_{12}$ thin films. *Journal of crystal growth*, 310(15), 3470-3473.

19. Pongpaiboonkul, S., Daniels, T.M., Hodak, J.H., Wisitsoraat, A. and Hodak, S.K. (2021). Preferentially oriented Fe-doped $CaCu_3Ti_4O_{12}$ films with high dielectric constant and low dielectric loss deposited on $LaAlO_3$ and $NdGaO_3$ substrates. *Applied Surface Science*, 540, 148373.

20. Sinclair, D.C., Adams, T.B., Morrison, F.D. and West, A.R. (2002). $CaCu_3Ti_4O_{12}$: One-step internal barrier layer capacitor. *Applied Physics Letters*, 80(12), 2153-2155.

21. Huang, Y., Wu, K., Xing, Z., Zhang, C., Hu, X., Guo, P., Zhang, J. and Li, J. (2019). Understanding the validity of impedance and modulus spectroscopy on exploring electrical heterogeneity in dielectric ceramics. *Journal of Applied Physics*, 125(8), 084103.

22. West, A.R., Adams, T.B., Morrison, F.D. and Sinclair, D.C. (2004). Novel high capacitance materials:-$BaTiO_3$: La and $CaCu_3Ti_4O_{12}$. *Journal of the European Ceramic Society*, *24*(6), 1439-1448.

23. Kumar, R., Zulfequar, M. and Senguttuvan, T.D. (2019). Improved giant dielectric properties in microwave flash combustion derived and microwave sintered $CaCu_3Ti_4O_{12}$ ceramics. *Journal of Electroceramics*, 42, 41-46.

24. Tan, Y.Q., Zhang, J.L., Hao, W.T., Chen, G., Su, W.B. and Wang, C.L. (2010). Giant dielectric-permittivity property and relevant mechanism of $Bi_{2/3}Cu_3Ti_4O_{12}$ ceramics. *Materials Chemistry and Physics*, 124(2-3), 1100-1104.

25. Riquet, G., Marinel, S., Bréard, Y. and Harnois, C. (2019). Sintering mechanism and grain growth in $CaCu_3Ti_4O_{12}$ ceramics. *Ceramics International*, 45(7), 9185-9191.

26. Yang, L., Huang, G., Wang, T., Hao, H. and Tian, Y. (2016). Colossal dielectric permittivity and relevant mechanism of $Bi_{2/3}Cu_3Ti_4O_{12}$ ceramics. *Ceramics International*, 42(8), 9935-9939.

27. Deng, J., Sun, X., Liu, S., Liu, L., Yan, T., Fang, L. and Elouadi, B. (2016). Influence of interface point defect on the dielectric properties of Y doped $CaCu_3Ti_4O_{12}$ ceramics. *Journal of advanced dielectrics*, 6(01), 1650009.

28. Imam, N.G., Abou Hasswa, M. and Okasha, N. (2021). Synchrotron X-ray absorption fine structure study and dielectric performance of $Li_{0.5}Fe_{2.5}O_4/BaTiO_3$ multiferroic. *Journal of Materials Science: Materials in Electronics*, 32(16), 21492-21510.

29. Kumar, A., Yadava, S.S., Singh, L., Verma, M.K., Singh, N.B. and Mandal, K.D. (2021). Enhancement of dielectric and magnetic properties of $0.5BaFe_{12}O_{19}$-$0.5Bi_{2/3}Cu_3Ti_4O_{12}$ nanocomposite synthesized via chemical route. *Journal of Magnetism and Magnetic Materials*, 527, 167807.

30. Masingboon, C., Thongbai, P., Maensiri, S. and Yamwong, T. (2009). Nanocrystalline $CaCu_3Ti_4O_{12}$ powder by PVA sol–gel route: synthesis, characterization and its giant dielectric constant. *Applied Physics A*, 96*,* 595-602.

31. Imam, N.G., Aquilanti, G., Azab, A.A. and Ali, S.E. (2021). Correlation between structural asymmetry and magnetization in Bi-doped $LaFeO_3$ perovskite: a combined XRD

and synchrotron radiation XAS study. *Journal of Materials Science: Materials in Electronics*, 32, 3361-3376.

32. Li, W. and Schwartz, R.W. (2007). Derivation and application of an empirical formula to describe interfacial relaxation effects in inhomogeneous materials. *Journal of the American Ceramic Society*, 90(11), 3536-3540.

33. Kong, S., An, Z., Zhang, W., An, Z., Yuan, M. and Chen, D. (2019). Preparation of hollow flower-like microspherical β-Bi_2O_3/BiOCl heterojunction and high photocatalytic property for tetracycline hydrochloride degradation. *Nanomaterials*, *10*(1), 57.

34. Jaiswar, S. and Mandal, K.D., 2017. Evidence of enhanced oxygen vacancy defects inducing ferromagnetism in multiferroic $CaMn_7O_{12}$ manganite with sintering time. *The Journal of Physical Chemistry C*, 121(36), 19586-19601.

35. Atuchin, V.V., Galashov, E.N., Khyzhun, O.Y., Kozhukhov, A.S., Pokrovsky, L.D. and Shlegel, V.N. (2011). Structural and electronic properties of $ZnWO_4$ (010) cleaved surface. *Crystal growth & design*, 11(6), 2479-2484.

36. Atuchin, V.V., Gavrilova, T.A., Grivel, J.C. and Kesler, V.G. (2008). Electronic structure of layered titanate $Nd_2Ti_2O_7$. *Surface science*, 602(19), 3095-3099.

37. Ren, L., Yang, L., Xu, C., Zhao, X. and Liao, R. (2018). Improvement of breakdown field and dielectric properties of $CaCu_3Ti_4O_{12}$ ceramics by Bi and Al co-doping. *Journal of Alloys and Compounds*, 768, 652-658.

38. Mansour, S.F., Imam, N.G., Goda, S. and Abdo, M.A. (2020). Constructive coupling between BiFeO3 and $CoFe_2O_4$; promising magnetic and dielectric properties. *Journal of Materials Research and Technology*, 9(2), 1434-1446.

39. Han, C.S., Choi, H.R., Choi, H.J. and Cho, Y.S., 2017. Origin of abnormal dielectric behavior and chemical states in amorphous $CaCu_3Ti_4O_{12}$ thin films on a flexible polymer substrate. *Chemistry of Materials*, 29(14), 5915-5921.

40. Godara, P., Agarwal, A., Ahlawat, N. and Sanghi, S. (2018). Crystal structure, dielectric and magnetic properties of Gd doped $BiFeO_3$ multiferroics. *Physica B: Condensed Matter*, 550, 414-419.

41. Adnan, S.B.R.S. and Mohamed, N.S. (2014). AC conductivity and dielectric studies of modified Li_4SiO_4 ceramic electrolytes. *Ceramics International*, 40(7), 11441-11446.

42. Ben Yahya, S. and Louati, B. (2021). Vibrational analysis and AC electrical conduction behavior of lithium zinc orthogermanate. *Ionics*, *27*(7), 3027-3034.

43. Yu, K., Tian, Y., Gu, R., Jin, L., Ma, R., Sun, H., Xu, Y., Xu, Z. and Wei, X. (2018). Ionic conduction, colossal permittivity and dielectric relaxation behavior of solid electrolyte $Li_{3x}La_{2/3-x}TiO_3$ ceramics. *Journal of the European Ceramic Society*, 38(13), 4483-4487.

44. Rai, V.S., Pandey, S., Kumar, V., Verma, M.K., Kumar, A., Singh, S., Prajapati, D. and Mandal, K.D. (2021). Investigation of microstructure and dielectric behavior of $Bi_{2/3}Cu_{3-x}Mg_xTi_4O_{12}$ (x= 0, 0.05, 0.1 and 0.2) ceramics synthesized by semi-wet route. *Journal of Materials Science: Materials in Electronics*, 32, 7671-7680.

45. Ren, L., Yang, L., Xu, C., Zhao, X. and Liao, R. (2018). Improvement of breakdown field and dielectric properties of $CaCu_3Ti_4O_{12}$ ceramics by Bi and Al co-doping. *Journal of Alloys and Compounds*, 768, 652-658.

46. Das, T. and Verma, B. (2019). Synthesis of polymer composite based on polyaniline-acetylene black-copper ferrite for supercapacitor electrodes. *Polymer*, 168, 61-69.